energies

MDPI

Article

Pressure-State-Aware Flexibility Assessment of Cascade Hydrogen Storage and Its Scheduling Implications

Wangquan He, Liqun Liu * and Qingfeng Wu

College of Electronic Information Engineering, Taiyuan University of Science and Technology, Taiyuan 030024, China; 2020002@tyust.edu.cn (Q.W.)
* Correspondence: llqd2004@163.com

Abstract

Total hydrogen inventory need not determine bounded-horizon station-side serviceability in a pressure-differentiated cascade. We examine this state-sufficiency question using a specified isothermal Noble–Abel three-bank model and a deterministic 24-part allocation lattice containing 221 pressure-feasible states. Two extremal states in the 55-state medium-inventory group each contain 328.418 kg, but their one-hour serviceable hydrogen reserves, SRH_{60}, are 24.000 and 54.237 kg. Their 30.237 kg difference is a model-bounded counterexample, not an estimate of operational prevalence. In a completed design-model sensitivity test, common multipliers of 0.8, 1.0 and 1.2 on the three-bank discharge caps give fixed-pair gaps of 25.600, 30.237 and 33.837 kg. The counterexample persists in these settings, but other equal-inventory pairs exhibit heterogeneous responses and ordering reversals. Composition-aware regression increases descriptive R^2 from 0.158 to 0.400, without establishing strong predictive performance. The existing four-bin test distinguishes equal-total 20 kg demand profiles, and the separate preparation/service test identifies 6–26 kg of pre-positioning for the low-reserve state at 30–50 kg requests, versus none for the high-reserve state. The results concern the specified station-side model; they do not validate equipment operating ranges, actual vehicle-received mass, field occurrence frequency or universal cost benefits.

Keywords: hydrogen refuelling station; cascade storage; serviceable hydrogen; state aggregation; Noble–Abel equation of state; static recourse feasibility

1. Introduction

Hydrogen refuelling stations (HRSs) must match intermittent hydrogen production and delivery with refuelling requests that arrive on a much shorter operational timescale. A typical station couples electricity supply, an electrolyser, compression and a set of pressure-differentiated storage banks to the dispensing process. Cascade arrangements exploit those pressure levels to supply vehicles while managing compression and storage requirements [1–8]. Their operation therefore has both a resource dimension—the hydrogen mass on site—and a service dimension—the mass that can cross the relevant pressure and flow constraints before a deadline.

Existing cascade studies have developed detailed representations of pressure-level selection, bank-volume allocation and compression configuration. Yu et al. [2] studied three-stage volume ratios, Xiao et al. [4] analyzed the energy consequences of pressure-level choices, and Reddi et al. [5] investigated station compression and storage sizing.

Academic Editor: Ivan Tolj

Received: 23 September 2026
Revised: 3 November 2026
Accepted: 16 November 2026
Published: 26 November 2026

Copyright: © 2026 by the authors. Licensee MDPI, Basel, Switzerland. This article is an open access article distributed under the terms and conditions of the Creative Commons Attribution (CC BY) license.

Filling-control and thermodynamic studies resolve operating sequences, cooling, tank trajectories or directly pressurized refuelling [1,3,9–12]. Recent work also considers infrastructure reliability and safety as drivers of hydrogen-refuelling-station development [13], while an AI-based framework has been compared with HOMER for autonomous-station techno-economic analysis [14]. These studies address important but different questions. The present contribution is not a new station architecture, equation of state or AI predictor; it tests whether total inventory is a sufficient state descriptor for a defined short-horizon service-feasibility decision. Cardona et al. [15] use an MLD framework with pressure-equilibrium-based hydrogen availability and two-tank sequential transfers. Their refuelling CSP uses arriving vehicles' initial onboard hydrogen mass, while nominal operation uses HMPC. Here, the question is instead an equal-inventory comparison within a finite 221-state lattice using a study-defined static station-side SRH_{60}; vehicle-side pressure equilibrium and sequential cascade discharge are not simulated.

At the integrated-energy-system scale, hydrogen production and storage are coordinated with electricity networks, renewable generation or local demand [16–28]. A single total-mass or state-of-charge variable is attractive in such schedules because it keeps the intertemporal hydrogen balance compact. That balance can be correct as resource accounting while leaving the immediate service capability of a cascade unresolved. The missing information becomes material when different bank allocations share the same total mass but face distinct pressure floors and discharge limits. Whether the aggregate state is adequate thus depends on the decision being made, not simply on whether hydrogen mass is conserved.

This study asks whether total inventory alone determines short-horizon station-side reserve under specified bank pressure floors and discharge-rate limits. It does not seek a new equation of state, station architecture or general scheduling algorithm. The primary evidence is an equal-inventory counterexample in a Noble–Abel-feasible design lattice. Pairwise counts describe that finite lattice, and regression is used only as a descriptive diagnostic. The existing sequential preparation/service test illustrates a consequence for a station-side service commitment. Completed discharge-cap sensitivity calculations test the same frozen states, while the pressure-window and volume tests rebuild their respective feasible lattices. These comparisons do not establish how often such states arise in operation or whether bank-resolved control is generally superior to existing pressure-aware formulations.

2. System Description and Problem Formulation

The modelled pathway is electricity or renewable supply to an electrolyser, compression into low-, medium- and high-pressure (LP, MP and HP) stationary storage, and a specified mass request. Bank pressure floors and bank-specific charge/discharge limits determine the mass available for service. The analysis is station-side: it does not resolve vehicle-tank pressure matching, precooling, nozzle flow or transient filling temperature [6,10,21,29].

The three banks are deliberately heterogeneous. Their volumes are 6.0, 3.0 and 2.0 m^3, and their permitted pressure ranges are 20–45, 45–70 and 70–90 MPa for LP, MP and HP, respectively. The corresponding discharge caps are 24, 18 and 14 kg h^{-1}; charge caps are 45, 30 and 20 kg h^{-1}. The electrolyser and compressor each have a 48 kg h^{-1} capacity, the station service cap is 92 kg h^{-1}, and pressure–mass calculations use 293.15 K. These are specified deterministic case parameters, not measurements from a commercial station. Table 1 records the same fixed inputs used throughout the comparisons.

Let the station inventory be the sum of the masses in its three banks. A total-mass state treats reallocations among LP, MP and HP as indistinguishable; a bank-resolved state retains those reallocations. In a one-hour service request, a bank contributes only the

lesser of its mass above the operational lower bound and the amount allowed by its discharge cap. The adequacy of aggregation is tested against this explicit service definition, with all device capacities, bounds, temperature and demand held fixed across the controlled state pair.

Table 1. Main parameters of the three-bank cascade case.

Parameter	LP	MP	HP	Unit	Source/Status
Volume	6.0	3.0	2.0	m^3	Specified case parameter
Pressure range	20–45	45–70	70–90	MPa	Specified case parameter
Discharge cap	24	18	14	kg h^{-1}	Specified case parameter
Charge cap	45	30	20	kg h^{-1}	Specified case parameter
Electrolyser capacity	48	—	—	kg h^{-1}	Specified case parameter
Compressor capacity	48	—	—	kg h^{-1}	Specified case parameter
Station service capacity	92	—	—	kg h^{-1}	Specified case parameter
Temperature	293.15	—	—	K	Specified case parameter

3. Materials and Methods

3.1. Bank-Resolved Cascade Storage Representation

Index i denotes an LP, MP or HP bank, and t indexes the dispatch interval. The state comprises bank mass $m_{i,t}$ (kg) and its associated pressure $P_{i,t}$ (Pa in the constitutive equations; MPa when the specified bounds are tabulated). V_i is bank volume (m^3). Bank-specific lower and upper masses follow from the pressure bounds under the chosen pressure–mass relation. The station-wide inventory $M_t = \Sigma_i m_{i,t}$ is a projection of this three-dimensional state, not a complete description of it. Two points with the same M_t can occupy different positions relative to each bank's lower service bound.

Hydrogen input and output are accounted for separately at each bank. A charge to one bank cannot be assumed to be serviceable from another without an explicit compression or transfer action. The model constrains charge and discharge by the stated bank caps and constrains the total action by compressor and station service capacities. This representation is sufficient for the controlled near-term service question; it does not specify valve sequencing or vehicle-filling transients.

3.2. Pressure–Mass Relationships and Operating Bounds

For comparison, the ideal-gas relation maps mass to pressure at a fixed temperature:

$$P_{i,t} = \left(\frac{R_{H_2} T}{V_i}\right) m_{i,t} \quad (1)$$

Here, R_{H2} is the specific gas constant of hydrogen (J kg^{-1} K^{-1}), T is absolute temperature (K), $m_{i,t}$ is stored mass (kg), and V_i is geometric bank volume (m^3). Because the ideal-gas approximation can be inaccurate at high hydrogen pressures, Equation (1) is retained only as a comparator; it is not used to generate the revised primary state lattice [30–31].

The primary pressure–mass mapping uses the isothermal Noble–Abel relation:

$$P_{i,t} = \frac{R_{H_2} T \rho_{i,t}}{1 - b\rho_{i,t}} \quad (2)$$

In Equation (2), $\rho_{i,t} = m_{i,t}/V_i$ is density (kg m^{-3}) and b is the covolume (m^3 kg^{-1}). We use b = 0.007691 m^3 kg^{-1}, as given in Section 4.1.1, Equation (15), of the HyRAM 1.0 Technical Reference Manual [31]. The manual reports density comparisons with NIST REFPROP in its applicability discussion; these published comparisons motivate the simplified closure but are not an independent accuracy validation performed in this study. The selected 20–90 MPa pressure windows and 293.15 K temperature are evaluated using this simplified isothermal Noble–Abel closure; this is a model-bounded calculation, not a claim of reference-EOS accuracy. Leachman et al. [30] provide a fundamental reference-fluid equation of state. Noble–Abel is selected for transparent, closed-form pressure-compatible mass bounds. Noble–Abel remains the primary closure. The additional CoolProp HEOS fixed-state comparison in Sections 3.10 and 4.6 examines limited model dependence; it is not a direct REFPROP software comparison, experimental property validation or a complete reference-EOS accuracy assessment. A transient vessel energy balance remains outside the present scope.

3.3. Short-Horizon Serviceable Hydrogen Metric

A bank mass balance governs the evolution of stored hydrogen:

$$m_{i,t+1} = m_{i,t} + \Delta t(q_{i,t,\text{in}} - q_{i,t,\text{out}}) \quad (3)$$

The interval duration Δt is in hours; $q_{i,t,\text{in}}$ and $q_{i,t,\text{out}}$ are bank charge and discharge rates (kg h^{-1}). Equation (3) is the interval-integrated mass balance for a bank with no leakage or venting term, with each flow rate interpreted as its average over the time interval. Piecewise-constant interval rates give the same update. Replenishment is an explicit action that changes a bank state rather than an implicit consequence of a large aggregate stock.

For a fixed initial state and horizon τ in hours, serviceable hydrogen is defined in this study as:

$$\text{SRH}_\tau = \sum_i \min\left(\max\left(m_i - m_{i,\min}, 0\right), q_{i,\text{out}}^{\max}\tau\right) \quad (4)$$

In Equation (4), m_i is the initial bank mass (kg), $m_{i,\min}$ is its mass at the lower pressure bound under Equation (2), and $q_{i,\text{out}}^{\max}$ is its discharge-rate cap (kg h^{-1}). The inner maximum excludes mass below the service floor; the outer minimum enforces the rate cap over horizon τ. SRH_τ is therefore a station-side, bounded-horizon deliverability metric in kilograms, not a prediction of the mass actually received by a vehicle. Total inventory $M = \Sigma_i m_i$ remains the appropriate resource-accounting quantity. Equation (4) is the reserve definition used in this study, rather than a vehicle-filling relation adopted from another model. The bank lower bounds are specified stationary-store operating limits, not thresholds calculated from a vehicle tank's initial or target pressure. Equation (4) has no vehicle-pressure matching or transient filling model; station-side reserve adequacy alone does not establish actual mass transfer into a vehicle.

The definition is static for the initial serviceable reserve. It excludes newly produced hydrogen unless a separate pre-positioning action is explicitly evaluated. A shorter horizon tightens each $q_{i,\text{out}}^{\max}\tau$ term: in the revised matched pair, SRH_{30} is 12 and 28 kg, compared with SRH_{60} of 24.000 and 54.237 kg. These are model-derived station-side values, not measured vehicle-fill quantities.

3.4. Designed State Lattice and Equal-Inventory Controlled Comparison

The primary states are generated directly from the Noble–Abel bank-mass bounds, whose total lower and upper inventories are 254.993 and 388.492 kg. The former 447.289 kg ideal-gas pair exceeds this model's total upper bound and is excluded from the primary analysis. Target totals are defined by $M_{\text{target}} = M_{\min} + f(M_{\max} - M_{\min})$, with f = 0.35, 0.55 and

0.75 prescribed as design levels in the construction code. These values describe positions within the feasible total-inventory interval, not measured operating levels, bank-specific states of charge or probabilities. The retained records do not establish a physical or operational rationale for choosing precisely these values. At each level, excess mass above the summed lower bounds is distributed using all non-negative integer triplets summing to 24. Triplets violating any bank upper mass bound are discarded, retaining 144 low-, 55 medium- and 22 high-inventory states. Results at untested fractions are not estimated, and discharge-cap sensitivity does not establish inventory-fraction sensitivity.

Within the medium-inventory group, the illustrative matched pair is selected by a transparent extremal rule: the state with a minimum SRH_{60} (M_{LR}) and the state with a maximum SRH_{60} (M_{HR}) among all 55 feasible allocations. Both contain 328.417541 kg. M_{LR} has LP/MP/HP masses of 161.481/86.814/80.123 kg and SRH_{60} = 24.000 kg; M_{HR} has 118.650/117.408/92.360 kg and SRH_{60} = 54.237 kg. Their pressures remain within the specified bank windows. This is an extremal counterexample, not a representative sample; the complete state-grid pair counts are reported separately. Data S1 contains all feasible states and the allocation triplets. Figure 1 summarizes the SRH_{60} distribution across the three inventory groups and marks M_{055} and M_{001}; horizontal jitter is used only to make overlapping states visible.

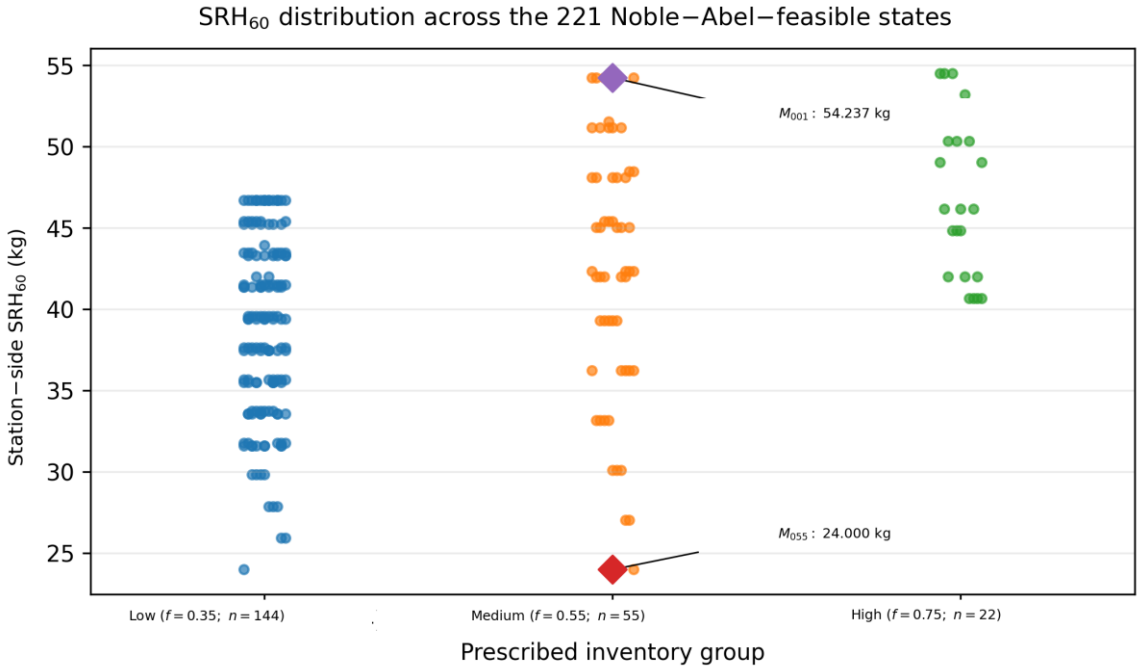


Figure 1. Distribution of SRH_{60} across the 221 Noble–Abel-feasible states. M_{055} (M_{LR}) and M_{001} (M_{HR}) are the minimum- and maximum-SRH_{60} states within the 55-state medium-inventory group; horizontal jitter is for visibility only.

3.5. Aggregate and Composition-Aware Diagnostic Models

The information-content diagnostic uses SRH_{60} from all 221 Noble–Abel-feasible states. Model A is ordinary least squares on total inventory alone. Model B adds HP and MP shares of total mass; the LP share is implicit because the three shares sum to one. The diagnostic compares predictors on the same deterministic state set. It is descriptive of this enumerated lattice, not inferential evidence from independent station observations.

R^2 and adjusted R^2 summarize in-sample fit; MAE and RMSE are measured in kilograms of SRH_{60}. Leave-one-out cross-validation (LOOCV) refits each model while withholding one enumerated state. Because these states are deterministically constructed

and not independent observations, we do not use a nested-test *p*-value as inferential evidence. Model B remains a weak-to-moderate explanatory diagnostic: it leaves most SRH_{60} variation unexplained. The equal-inventory physical counterexample, not the regression, is the primary evidence.

3.6. Predefined Scheduling Stress Test

The scheduling analysis has two distinct parts. First, a no-action four-bin profile test holds total demand at 20 kg over four 15 min intervals and compares Uniform [5,5,5,5], Front-loaded [8,6,4,2], and Back-loaded [2,4,6,8] kg profiles. Each bin must be served within that interval; queueing is not allowed. This isolates profile timing because both matched states have SRH_{60} above 20 kg, while the low-reserve state has serviceable mass only in LP and an LP limit of 6 kg per 15 min. The aggregate-only comparator uses the summed 56 kg h^{-1} discharge ceiling (14 kg per 15 min bin) and therefore regards all three profiles as feasible. Second, an aggregate one-hour request stress test evaluates total requests of 30, 35, 40, 45 and 50 kg and the minimum pre-positioning needed under bank constraints. The earlier four-step implementation did not encode time-varying demand; the explicit profile test is the basis for the revised timing result.

Recourse is defined here as the minimum additional hydrogen mass x_i (kg) pre-positioned in bank i during a separate preparation period before the service commitment; y_i (kg) is the additional mass deliverable from that bank during the subsequent service horizon. The feasibility calculation minimizes $\Sigma_i x_i$ subject to $0 \le y_i \le x_i$, $x_i \le q_{i,\mathrm{ch,max}}\,\tau_p$, $x_i \le m_{i,\max} - m_i$, $y_i \le \max(0, q_{i,\mathrm{out,max}}\,\tau_s - s_{i0})$, $\Sigma_i y_i \ge \max(0, D - SRH_{60})$, and $\Sigma_i x_i \le \min(C_{\mathrm{comp}}, C_{\mathrm{el}})\tau_p$. Here, s_{i0} is the initial contribution of bank i to SRH_{60}, and $\tau_p = \tau_s = 1$ h are the preparation and service horizons, respectively; these are sequential periods, not a simultaneous dynamic dispatch. The station service cap is non-binding because the sum of bank discharge caps is 56 kg h^{-1}. The objective and constraints above are specified for this study's static pre-positioning feasibility test; they are not asserted to be a formulation adopted from references [1] or [7]. This static test does not resolve within-hour production, compression and dispensing trajectories.

The recourse calculation is implemented in the accompanying deterministic Python script. Whenever feasible, the minimum total pre-positioning equals the no-action shortfall; a deterministic MP → HP → LP allocation provides a feasibility witness subject to bank charge limits, storage headroom, residual discharge capacity, electrolyser capacity and compressor throughput. The bank allocation is not selected by an economic objective and is not claimed to be an optimal operating policy. The script provides state enumeration, pressure–mass conversion, SRH calculation, profile feasibility, recourse feasibility and sensitivity calculations for independent reproduction.

3.7. Pressure-Boundary, Storage-Volume and Discharge-Cap Sensitivity

The sensitivity analysis changes one parameter family at a time while rebuilding the feasible medium-inventory simplex. First, all lower and upper pressure-window boundaries are shifted jointly by −5 and +5 MPa, preserving each bank's pressure-window width. Second, all three-bank volumes are scaled uniformly by 0.8 and 1.2. The same 24-part allocation rule and bank-specific discharge caps are retained. These tests assess the persistence of the state gap under specified perturbations; they are not an uncertainty distribution or a substitute for station data.

Compressor capacity is varied at 12, 24, 36 and 48 kg h^{-1}. For M_{LR}, the static pre-positioning test is feasible at 12 kg h^{-1} for 30 and 35 kg requests, at 24 kg h^{-1} for 30–45 kg requests, and at 36 or 48 kg h^{-1} for all five tested requests through 50 kg. M_{HR} requires no pre-positioning for any tested request. Feasibility remains conditional on bank charge-rate limits, remaining storage headroom, residual bank discharge capability and electrolyser

capacity. This is request-magnitude and compressor-capacity sensitivity, not a validation across real vehicle-arrival profiles.

A separate discharge-cap sensitivity test applies a common multiplier $\alpha \in \{0.8, 1.0, 1.2\}$ to the LP, MP and HP discharge caps of 24, 18 and 14 kg h^{-1}, respectively. These remain separate bank constraints, rather than a single station-wide cap. The scenarios are local perturbations of specified design-model inputs, not calibrated equipment operating ranges. The same 221 initial Noble–Abel-feasible states, bank volumes, temperature, pressure bounds, inventory levels and bank-mass allocations are retained. SRH_{60} is evaluated over a one-hour no-action service window. The fixed pair remains $M_{LR} = M_{055}$ and $M_{HR} = M_{001}$; it is not reselected at each multiplier. All 12,012 unordered equal-inventory pairs are compared within their original inventory groups. For ordering comparisons, the same state-ID orientation is retained at each setting; a strict reversal means that the signed SRH_{60} difference changes sign between the baseline and the perturbed setting. Zero differences are reported separately. This test does not calculate new pre-positioning actions, compressor schedules or vehicle-filling trajectories.

3.8. Computational Implementation and Reproducibility

The revised primary state lattice, pressure and SRH calculations, pairwise counts, descriptive regressions, demand/recourse feasibility checks and one-factor sensitivities are reproduced by the accompanying Python script using NumPy and pandas. It enumerates all non-negative integer triplets on a 24-part simplex and discards states that violate Noble–Abel bank-mass bounds. No random seed or field data are used. The recourse calculation is a static linear feasibility problem, not a full dynamic optimization. The previous 72-state ideal-gas subset and its historical post hoc remapping are retained only as audit history and are not the basis of the revised primary results.

The computational sequence is: calculate Noble–Abel bank mass bounds; enumerate all feasible 24-part allocations at the three stated inventory fractions; compute bank pressures and SRH_{30}/SRH_{60}; select the minimum- and maximum-SRH_{60} states within the medium-inventory group; calculate pairwise lattice statistics; fit the aggregate-only and composition-aware descriptive regressions on all 221 feasible states; evaluate the three four-bin 20 kg profiles; evaluate five aggregate request magnitudes at four compressor capacities; and repeat the lattice comparison after joint pressure-window shifts and uniform volume scaling. In addition, retain the same 221 states while recalculating SRH_{60} under common discharge-cap multipliers of 0.8, 1.0 and 1.2, then compare all within-group pairs for absolute-gap changes, nonzero-to-zero transitions and strict ordering reversals. The supplied script regenerates the numerical CSV outputs, including Data S8–S10, from the stated parameters. No field data or random scenario generation enters the analysis.

The revised 221-state analysis is a direct reconstruction under Noble–Abel bank bounds, not a replay of the earlier pressure-compatible remapping. The original 72-state ideal-gas analysis and its 32.00 kg example are distinct from the revised matched pair at 328.417541 kg and its 30.237464240 kg gap. Archived historical remapping outputs do not by themselves establish the complete transformation procedure. They are not substituted for the revised primary states or presented as a reproduced historical algorithm.

3.9. Use of Generative AI Tools

During manuscript preparation and revision, OpenAI ChatGPT was used primarily for research discussion, analysis, and suggestions. It also assisted with research-workflow organization, manuscript and reviewer-response drafting and editing, and consistency checks. The authors made the final research-design decisions. The original MATLAB/Python numerical analyses were primarily carried out by the authors. The available records do not establish a complete step-by-step attribution of every original

regression and scheduling design, coding, execution, and interpretation task to a particular author or AI tool. During the revision-stage audit, OpenAI Codex was used to inspect archived code and data, reproduce documented deterministic calculations, compare numerical outputs, and prepare audit reports and logs. The authors checked the equations, key numerical results, data, and model assumptions and retain responsibility for the scientific content, interpretations, and conclusions.

3.10. EOS Comparison Protocol

To examine whether the identified station-side reserve difference depends entirely on the Noble–Abel pressure–mass closure, a fixed-state comparison was conducted using HEOS::Hydrogen in CoolProp version 8.0.0 (Python 3.13.9) [30,32]. The previously selected states M_{055} and M_{001} were retained without changing their original LP, MP or HP bank-mass allocations or their equal total inventory of 328.417541 kg. Temperature was 293.15 K; LP/MP/HP volumes were 6, 3 and 2 m^3, their pressure intervals were 20–45, 45–70 and 70–90 MPa, and discharge caps were 24, 18 and 14 kg h^{-1}, respectively. The original MATLAB calculations were performed using MATLAB R2024b. The Data S1–S10 Python reproduction script requires Python 3.10 or later; the exact interpreter version used for its original execution was not retained in the available records.

The Noble–Abel implementation retained R_{H2} = 4124 J kg^{-1} K^{-1} and b = 0.007691 m^3 kg^{-1}. HEOS used the native Hydrogen molar mass of 0.00201588 kg mol^{-1} and molar gas constant of 8.314472 J mol^{-1} K^{-1}. Thus, the test compares two complete pressure–mass model configurations rather than an isolated covolume-parameter perturbation. The recorded backend was HelmholtzEOSBackend; software metadata were are supplied with the EOS addendum.

In the primary fixed-mass comparison, each bank pressure was obtained from its unchanged mass density and temperature. HEOS used AbstractState with DmassT_INPUTS, without forced phase selection. Strict feasibility required all three pressures to lie within their respective closed intervals before the reserve was evaluated. Equation (4), its one-hour horizon and the discharge caps were unchanged; only the EOS-dependent mass at each lower pressure boundary changed. A separate secondary fixed-pressure diagnostic used PT_INPUTS at each bank boundary to obtain density and mass. It is a boundary-mapping diagnostic, not a new matched-state SRH_{60} comparison.

The stored pressure and mass round-trip checks used external acceptance thresholds of 1 Pa and 10^{-6} kg. Strict closed-interval feasibility and the 1 Pa numerical-boundary classification were recorded separately; neither threshold establishes physical property accuracy or the native internal iteration tolerance, which was not exposed. The comparison did not reconstruct the 221-state lattice, reselect its extrema, estimate station occurrence frequencies, calculate new recourse actions or simulate vehicle filling. Data S11–S14B in the independent EOS supplementary addendum preserve the full-precision inputs and results.

4. Results

4.1. Equal-Inventory Non-Equivalence

Does the same station-wide mass imply the same one-hour service reserve? Table 2 compares the two extremal states within the medium-inventory group. Both contain 328.418 kg under the same Noble–Abel pressure–mass relation, yet M_{LR} has SRH_{60} = 24.000 kg and M_{HR} has SRH_{60} = 54.237 kg, a 30.237 kg gap. Their SRH_{30} values are 12 and 28 kg. This counterexample follows directly from bank pressure floors and rate caps, before any fitted diagnostic model is introduced. Figure 2 illustrates this matched-state reserve difference.

Table 2. Equal-inventory physical evidence for the extremal M_{LR} and M_{HR} states.

Metric	M_{LR} (Minimum SRH_{60})	M_{HR} (Maximum SRH_{60})	Difference/Interpretation
Total inventory (kg)	328.418	328.418	0 kg; matched under Noble–Abel
SRH_{30} (kg)	12.000	28.000	16.000 kg difference
SRH_{60} (kg)	24.000	54.237	30.237 kg difference
Pressure bounds	All banks within bounds	All banks within bounds	Noble–Abel, 293.15 K
Selection rule	Minimum SRH_{60}	Maximum SRH_{60}	Extrema among 55 medium-group states

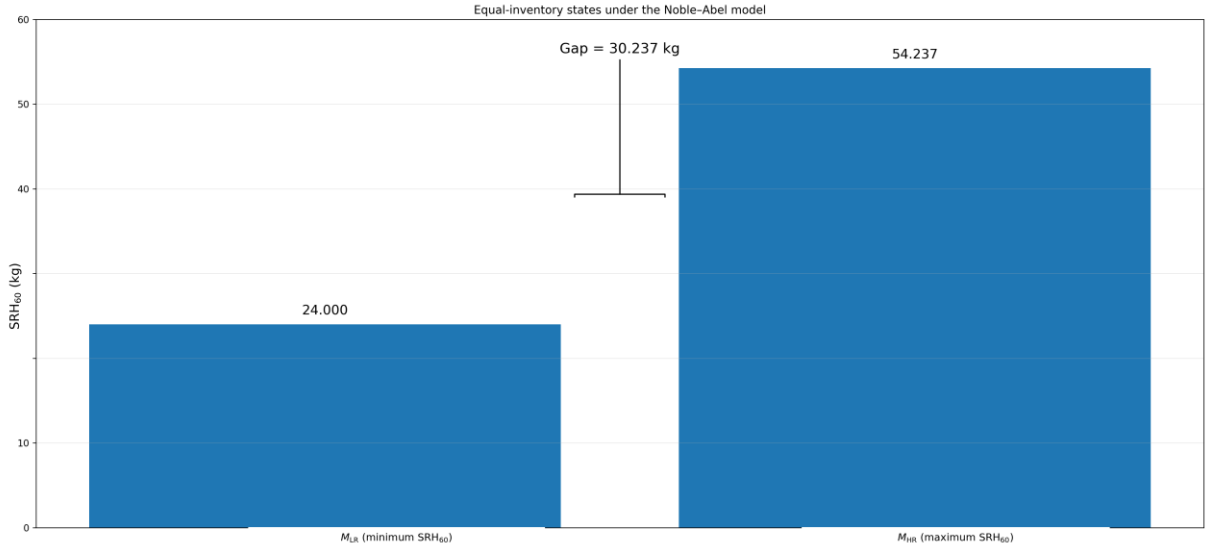


Figure 2. Equal-inventory SRH_{60} difference for the extremal medium-inventory states under the Noble–Abel model.

M_{LR} has LP at 41.030 MPa and MP/HP at their lower pressure bounds, so only the LP discharge cap contributes to its initial one-hour reserve. M_{HR} distributes the same total mass across all three banks so that LP, MP and HP each contribute to SRH_{60}. The difference is caused by bank composition under the same pressure and rate constraints, not by a difference in total inventory.

Across all within-group equal-inventory pairs in the revised 221-state lattice, SRH_{60} differences greater than 10 kg occur in 1948/10,296 low-inventory pairs, 524/1485 medium-inventory pairs and 28/231 high-inventory pairs (2500/12,012 overall). These are finite-grid coverage counts, not operating probabilities or independent observations; they do not provide the historical 72-state ideal-gas pairwise distribution.

4.2. Information Loss in Aggregate-State Representation

How much of the enumerated SRH_{60} variation is represented by total mass alone? Across 221 feasible states, Model A has $R^2 = 0.157907$ and adjusted $R^2 = 0.154062$. Model B, which additionally retains HP and MP mass shares, has $R^2 = 0.400490$ and adjusted $R^2 = 0.392202$. In-sample MAE decreases from 5.007884 to 4.278271 kg and RMSE from 6.076636 to 5.127215 kg. The increase in R^2 is 0.242583, but Model B still leaves approximately 60% of the response variation unexplained. These are descriptive diagnostics on a deterministic grid.

The LOOCV diagnostic is directionally consistent: MAE falls from 5.052097 to 4.357753 kg and RMSE from 6.128101 to 5.227411 kg when the composition terms are added. We do not report a nested-test *p*-value because the state set is deterministic rather than an independent sample. Table 3 and Figure 3 summarize the descriptive comparison. The physical equal-inventory contrast remains the primary evidence; the regression neither establishes field-wide prevalence nor a causal effect.

Table 3. Descriptive regression diagnostics over the 221-state feasible lattice.

Metric	Aggregate State (A)	Composition-Aware State (B)
R^2	0.157907	0.400490
Adjusted R^2	0.154062	0.392202
MAE (kg)	5.007884	4.278271
RMSE (kg)	6.076636	5.127215
LOOCV MAE (kg)	5.052097	4.357753
LOOCV RMSE (kg)	6.128101	5.227411
ΔR^2 vs. A	—	0.242583

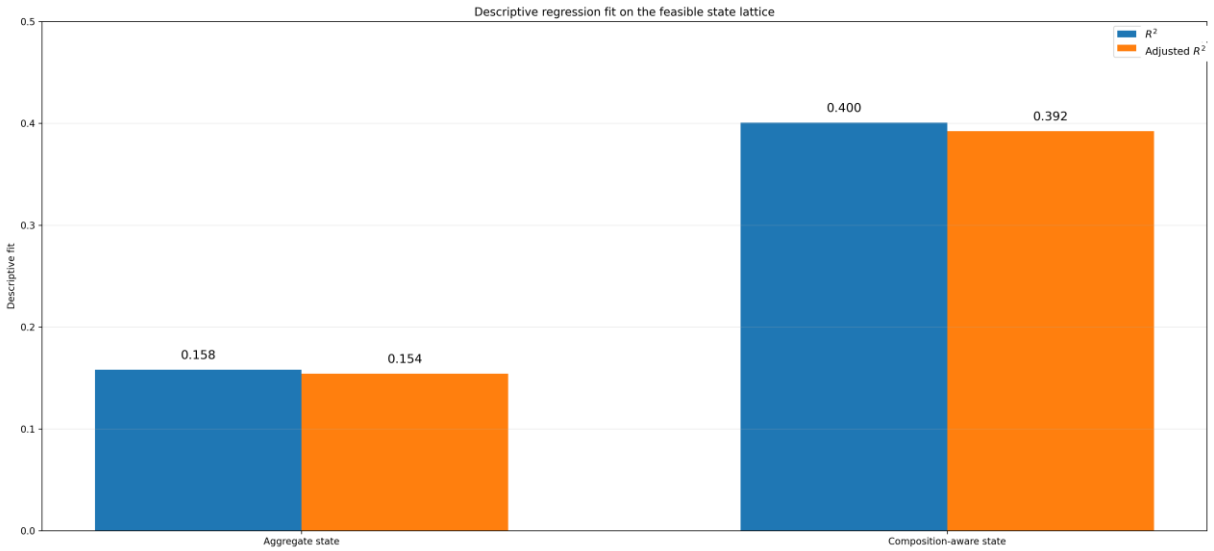


Figure 3. Descriptive R^2 and adjusted R^2 for aggregate and composition-aware state representations.

Both the predictors and SRH_{60} labels originate from the same deterministic state construction. The comparison diagnoses information retained by two feature sets; it is not independent validation of the physical metric. The mass-floor truncations and discharge-cap saturation in the SRH definition produce a piecewise response that need not be captured fully by the specified linear features. This is a structural explanation, not a tested attribution of residual variance to external factors. Temperature and device parameters are fixed in this dataset, so unmeasured vehicle conditions or operating noise cannot be invoked to explain its residuals. LOOCV withholds states within the same construction and does not establish transfer to measured stations. Model B's R^2 of 0.400490 and LOOCV RMSE of 5.227411 kg therefore do not establish strong predictive capability or economic value.

4.3. Scheduling Consequences

To isolate intra-hour timing from total demand, a separate no-action test uses three four-bin profiles with the same 20 kg total. The aggregate-only comparator regards all profiles as feasible because each bin is below its 14 kg aggregate rate ceiling. Under bank-specific limits, M_{LR} serves the uniform profile but cannot serve the front-loaded or back-loaded profile because an 8 kg bin exceeds the LP bank's 6 kg per-bin limit; M_{HR} serves all three. Demand must be met within each 15 min bin, with no queueing. This is a station-side rate/reserve test, not a vehicle-fill simulation. Table 4 summarizes the demand profiles and feasibility outcomes.

Table 4. Equal-total 20 kg demand-profile feasibility over four 15 min intervals.

Profile	Demand per 15 min (kg)	Aggregate-Only	M_{LR}	M_{HR}
Uniform	[5, 5, 5, 5]	Feasible	Feasible	Feasible
Front-loaded	[8, 6, 4, 2]	Feasible	Infeasible (bin 1)	Feasible
Back-loaded	[2, 4, 6, 8]	Feasible	Infeasible (bin 4)	Feasible

Does the missing state information affect a near-term action? The AGG representation predicts no recourse for both states at requests of 30, 35, 40, 45 and 50 kg because each request is below its assumed 56 kg aggregate discharge ceiling. The bank-resolved test instead requires 6, 11, 16, 21 and 26 kg of pre-positioning for M_{LR}; M_{HR} requires none at these demand levels because its SRH_{60} is 54.237 kg. This is a feasibility difference under the specified assumptions, not an estimate of general operating-cost savings.

At a 40 kg request, AGG predicts no intervention from either 328.418 kg total stock. The bank-resolved no-action check finds only 24 kg serviceable from M_{LR}, leaving 16 kg unserved; M_{HR} can serve all 40 kg. The static recourse test identifies 16 kg of pre-positioning for M_{LR} and none for M_{HR}. A deterministic allocation witness assigns 16 kg to MP at this request; at 45 and 50 kg it assigns MP 18 kg plus HP 3 and 8 kg, respectively. These are feasible allocations, not economically optimized choices. Table 5 summarizes the demand-level results.

Table 5. Demand-level sensitivity and static minimum-recourse feasibility for the matched Noble–Abel states.

D (kg)	AGG Action	M_{LR} SRH_{60} (kg)	M_{LR} Shortfall/Recourse (kg)	M_{HR} SRH_{60} (kg)	M_{HR} Shortfall/Recourse (kg)
30	No recourse	24.000	6.000	54.237	0.000
35	No recourse	24.000	11.000	54.237	0.000
40	No recourse	24.000	16.000	54.237	0.000
45	No recourse	24.000	21.000	54.237	0.000
50	No recourse	24.000	26.000	54.237	0.000

4.4. Pressure-Boundary and Storage-Volume Sensitivity

We tested two one-factor sensitivities on the medium-inventory grid. Jointly shifting all bank pressure-window boundaries by −5 or +5 MPa leaves the maximum equal-inventory SRH_{60} gap between 29.645 and 30.876 kg. Uniformly scaling all three-bank volumes by 0.8 or 1.2 leaves the gap between 27.790 and 32.000 kg. Table 6 reports the corresponding finite-grid pair counts. These calculations support persistence of the mechanism under the tested parameter changes; they do not validate transient filling or thermal behaviour.

Table 6. Sensitivity of the maximum equal-inventory SRH_{60} gap within the medium-inventory group.

Sensitivity	Setting	Medium-Group Total (kg)	Maximum SRH_{60} Gap (kg)	Pairs Differing by >10 kg
Pressure-window shift	−5 MPa	300.416	30.876	529/1485 (35.6%)
Pressure-window shift	+0 MPa	328.418	30.237	524/1485 (35.3%)
Pressure-window shift	+5 MPa	355.051	29.645	524/1485 (35.3%)
Uniform volume scale	0.8×	262.734	27.790	500/1485 (33.7%)
Uniform volume scale	1.0×	328.418	30.237	524/1485 (35.3%)
Uniform volume scale	1.2×	394.101	32.000	656/1485 (44.2%)

4.5. Discharge-Cap Sensitivity

The frozen matched pair has the same total inventory of 328.417541 kg in every discharge-cap setting. At α = 0.8, 1.0 and 1.2, M_{LR} has SRH_{60} of 19.200, 24.000 and 28.800 kg, while M_{HR} has 44.800, 54.237464240 and 62.637464240 kg. The corresponding differences are 25.600000000, 30.237464240 and 33.837464240 kg. A 40 kg station-side request remains infeasible without action for M_{LR} and feasible for M_{HR} in all three settings. The no-action shortfalls of 20.8, 16.0 and 11.2 kg are not newly optimized recourse amounts.

Each setting retains 221 states and 12,012 equal-inventory pairs: 10,296 low-, 1485 medium- and 231 high-inventory pairs. Relative to α = 1.0, the absolute difference decreases for 5541 pairs at α = 0.8 and 6476 pairs at α = 1.2. Previously nonzero differences become zero for 104 and 794 pairs, respectively, while strict ordering reversals occur for 685 and 82 pairs. These event counts are not mutually exclusive categories to be added together. The fixed counterexample therefore persists, but neither every pairwise difference nor every state ordering is invariant to discharge caps. The pairs share states and are not independent statistical samples. Table 7 summarizes the fixed-pair reserve values under the three discharge-cap settings.

Table 7. Fixed-pair discharge-cap sensitivity under the Noble–Abel design model.

Multiplier α	LP/MP/HP Discharge Caps (kg h^{-1})	M_{LR}/M_{HR} SRH_{60} (kg)	Gap HR–LR (kg)
0.8	19.2/14.4/11.2	19.200/44.800	25.600
1.0	24/18/14	24.000/54.237	30.237
1.2	28.8/21.6/16.8	28.800/62.637	33.837

4.6. Fixed-State EOS Comparison

Table 8 compares the two unchanged mass states under the two EOS configurations. Both states remain strictly three-bank feasible under HEOS. M_{055} and M_{001} have HEOS static SRH_{60} values of 25.071 and 54.976 kg, compared with 24.000 and 54.237 kg under Noble–Abel. Their positive reserve difference changes from 30.237 to 29.906 kg, a reduction of approximately 0.332 kg or 1.0971% relative to the Noble–Abel gap. This percentage compares two model-derived reserve differences; it is not an uncertainty interval, statistical-significance measure or property-accuracy bound.

M_{055} and M_{001} were selected as the reserve extrema in the original Noble–Abel medium-inventory lattice; they were not reselected as HEOS extrema. The positive fixed-pair difference therefore persists in the tested HEOS configuration, but this does not establish EOS robustness over all 221 states or their pairwise orderings. SRH_{60} remains a static station-side reserve proxy rather than actual vehicle-received mass or a sequential cascade-filling simulation.

All 24 stored numerical round-trip checks passed, with maximum absolute pressure and mass residuals of $1.4901161193847656 \times 10^{-8}$ Pa and $5.684341886080802 \times 10^{-14}$ kg. Two secondary boundary back-calculations slightly exceed their exact upper bank boundaries

while passing the 1 Pa round-trip criterion; these returned values are not classified as strictly pressure-feasible. They are distinct from the strictly feasible primary fixed-mass states. Data S11–S14B preserve the pressures, margins, classifications and numerical checks.

Table 8. Fixed-mass EOS comparison for the original Noble–Abel-selected pair; pressures and reserves are displayed to three decimal places.

State	EOS	LP Pressure (MPa)	MP Pressure (MPa)	HP Pressure (MPa)	Strict Three-Bank Feasibility	SRH_{60} (kg)
M_{055}	Noble–Abel	41.030	45.000	70.000	Yes	24.000
M_{055}	HEOS	41.177	45.226	70.962	Yes	25.071
M_{001}	Noble–Abel	28.195	67.687	86.580	Yes	54.237
M_{001}	HEOS	28.178	68.568	88.152	Yes	54.976

5. Discussion

5.1. Physical Interpretation of Equal-Inventory Non-Equivalence

A station-wide balance counts each kilogram once regardless of its location. A cascade cannot necessarily exchange those kilograms across banks within the request horizon. The pressure floor limits how much of a bank's mass is usable at all; its discharge cap limits how quickly the usable part can be supplied. A high total can therefore coexist with a small near-term service reserve. The equal-inventory comparison isolates this effect: changes in bank allocation alter the sum of constrained deliverable masses while leaving the total unchanged. This is a state-representation result, not merely a numerical comparison between two cases.

The mechanism also explains the horizon dependence. For sufficiently short τ, $q_{i,\mathrm{out}}{}^{\max}\tau$ can bind before the pressure-floor reserve is exhausted. As τ increases, the rate ceiling relaxes relative to available mass, although pressure floors may continue to bind. Replenishment, if scheduled, can further change the state during the horizon. SRH_{τ} therefore answers a specific service question, whereas total inventory remains the appropriate accounting quantity for mass conservation. Confusing the two quantities is the source of the no-action error observed in the stress window.

The discharge-cap results reveal heterogeneity between state pairs. In this model, each bank contribution is limited by either mass above its pressure floor or its horizon-specific discharge allowance. Changing a cap can switch the active limitation differently across states because accessible mass is distributed differently among banks. Thus, although relaxing discharge caps cannot reduce an individual state's reserve under this definition, a difference between two states need not retain its magnitude or sign. The observed ordering reversals preclude treating a particular bank allocation as uniformly preferable. They do not remove the fixed-pair existence counterexample under the three tested settings.

5.2. Relation to Existing Cascade Hydrogen Storage Studies

The present question complements, rather than replaces, cascade design and refuelling analyses. Prior studies evaluate pressure levels, vessel-volume allocation, energy use, storage utilization, filling control and vehicle-side dynamics [1–12]. The infrastructure-safety study by Frolova and Zhdaneev [13] addresses reliability, safety and technological development; Oueslati [14] compares an AI prediction/optimization framework with HOMER for autonomous-station techno-economic analysis. Neither topic is the same as the present finite-state sufficiency test. The contribution here is narrower: under a matched total inventory, does suppressing bank composition lose information relevant to a bounded-horizon service-feasibility decision? Cardona et al. [15]

already connect multi-tank availability with pressure equilibrium; their two-step availability construction and arrival-conditioned CSP are not equivalent to our static reserve operator. We therefore do not claim to introduce pressure-aware storage, multi-tank state modelling or pressure-equilibrium-based availability. The distinction is the controlled equal-inventory comparison under our stated static definition, not a demonstrated performance advantage over their controller. This is a literature comparison, not an implemented external benchmark. The full-method evidence gaps for references [13–14] remain unresolved.

Integrated-energy-system and HRS scheduling studies often emphasize electricity–hydrogen coordination, planning, renewable integration, uncertainty or learning-based control [13–14,16–28]. These approaches answer broader system or prediction questions. A scalar inventory remains useful for long-horizon resource accounting, but it may be insufficient for a time-critical service commitment when bank pressure and rate constraints bind. The present study therefore offers a conditional counterexample to scalar service-state sufficiency; it does not imply that existing scheduling models or cascade designs are generally invalid.

5.3. Implications for Hydrogen Refuelling Station and H-IES Scheduling

AGG is an internal information-restriction comparator: it retains total inventory and the summed discharge ceiling but omits bank composition. At the baseline 40 kg request, it predicts no intervention from either state, whereas the bank-resolved no-action reserve is insufficient for M_{LR} and sufficient for M_{HR}. The separate one-hour preparation test identifies 16 kg of pre-positioning for M_{LR} and none for M_{HR} under the specified capacity constraints. This is not a comparison with every scheduling model used in practice.

A validated conservative reserve constraint might avoid this particular aggregation error without retaining all bank states, but that alternative has not been tested. The present evidence does not quantify the incremental computation, operating-cost benefit or control-policy value of adopting a richer state. Establishing those trade-offs requires a reproducible external formulation and a matched computational comparison; E1 execution times and regression error reductions are not substitutes.

5.4. When Aggregate Inventory May Still Be Sufficient

Bank-resolved scheduling is not always necessary. If a model is used only for long-horizon resource accounting, the station-wide mass balance remains informative. Aggregate inventory may also be adequate for a particular service request when bank pressure floors are non-binding, accessible reserve exceeds the request with a margin, or replenishment and redistribution can be completed within the decision horizon under verified capacities. Likewise, a system without heterogeneous pressure or rate constraints would not exhibit the same mechanism. These are conditional sufficiency statements: they require checking the relevant bounds rather than inferring feasibility from total mass alone.

The value of a richer state rises when service obligations are time-critical and bank asymmetry is binding. At a planning resolution much coarser than the replenishment timescale, scalar stock can remain an efficient approximation. The present study does not establish a preferred dispatch interval or universal model size; it identifies a state-resolution question that should be checked against the intended service commitment.

5.5. Limitations and Transferability

The absence of measured station pressure–flow trajectories and vehicle-side filling data prevents estimation of operating frequencies and validation of vehicle-received hydrogen mass. The 221 states form a deterministic feasible lattice, and their pairwise counts describe design-grid coverage rather than a population distribution. Discharge-

cap multipliers of 0.8, 1.0 and 1.2 are design-model perturbations, not measured equipment ranges. The fixed pair retains its reserve gap, but other pairs show disappearing differences and ordering reversals. Untested inventory fractions and cascade configurations are not evaluated.

The isothermal Noble–Abel closure remains the primary model and provides transparent pressure-compatible mass bounds. The additional HEOS comparison covers only the two previously selected fixed-mass states; no full HEOS feasible-state-space enumeration, direct REFPROP software comparison, experimental property validation or complete reference-EOS accuracy assessment was performed. The model lacks vehicle initial and target pressures, bank-to-vehicle pressure-dependent flow, precooling and transient vehicle-tank thermodynamics. Bank operating floors are not vehicle-dependent pressure-matching thresholds. SRH_{60} is a station-side reserve metric, not certified vehicle-fill feasibility. The equal-total four-bin test and sequential preparation/service test remain simplified feasibility examples, not measured arrival processes, economic dispatch or a validated operating policy. A reproducible external scheduling benchmark and a fair AGG/PS computational-cost comparison are also not provided. REFPROP software itself was not used in this study; therefore, no REFPROP software version applies.

6. Conclusions

Within the specified Noble–Abel three-bank model, equal total inventory does not uniquely determine one-hour station-side reserve. Two extremal medium-inventory states each contain 328.418 kg but have SRH_{60} of 24.000 and 54.237 kg. Their reserve difference persists when the bank discharge caps are jointly multiplied by 0.8, 1.0 and 1.2. Other equal-inventory pairs respond heterogeneously and can reverse ordering, so the result is an existence counterexample, not a claim that one allocation is uniformly preferable.

The separate preparation/service example illustrates a conditional intervention difference; regression provides secondary descriptive evidence rather than strong operational prediction. Total inventory remains valid for mass accounting. The evidence does not establish real-station frequencies, calibrated equipment ranges, vehicle-received mass, universal cost benefits or the results at untested inventory fractions. Wider application requires station measurements, vehicle-side physical validation and reproducible operational comparisons.

Supplementary Materials: The following supporting information can be downloaded at https://www.mdpi.com/article/10.3390/en19235744/s1: The complete supplementary package contains Data S1–S10, comprising the original Noble–Abel state lattice, matched-pair data, pairwise statistics, descriptive regression diagnostics, demand/profile and static recourse tests, pressure/volume sensitivity, discharge-cap sensitivity and associated numerical outputs. The Data S1–S10 module is accompanied by the original deterministic Python reproduction script (reproduce_submission_results.py), README, requirements, method note, reproduction summary and file manifest. The independent EOS supplementary addendum contains Data S11 (fixed-mass EOS comparison), Data S12 (fixed-pressure boundary mapping), Data S13 (EOS round-trip validation), Data S14A (state feasibility) and Data S14B (SRH_{60} EOS comparison), together with software metadata and explanatory documentation. The EOS addendum provides stored model-derived records and numerical checks; it does not include the original Stage 9.3 EOS execution scripts and is not a portable, independently rerunnable EOS package. Data S12 is a pressure-boundary diagnostic, not a matched-state SRH_{60} comparison. The package contains the following 15 named data modules: Data S1: Noble–Abel feasible state lattice; Data S2: matched equal-inventory pair; Data S3: pairwise grid statistics; Data S4: descriptive regression diagnostics; Data S5: demand/recourse/compressor sensitivity; Data S6: temporal-profile sensitivity; Data S7: pressure/volume sensitivity; Data S8: discharge-cap sensitivity; Data S9: discharge-cap state results;

Data S10: discharge-cap pair transitions; Data S11: fixed-mass EOS comparison; Data S12: fixed-pressure boundary mapping; Data S13: EOS round-trip validation; Data S14A: state feasibility; Data S14B: SRH60 EOS comparison. No separately numbered supplementary items titled Figure S1, Table S1, or Video S1 are included in this package; therefore, captions for these items are not applicable.

Author Contributions: Conceptualization, W.H. and L.L.; methodology, W.H.; software, W.H.; validation, W.H., L.L. and Q.W.; formal analysis, W.H.; investigation, W.H.; data curation, W.H.; writing—original draft preparation, W.H.; writing—review and editing, L.L. and Q.W.; visualization, W.H.; supervision, L.L. and Q.W.; project administration, L.L. All authors have read and agreed to the published version of the manuscript.

Funding: This research was funded by the National Natural Science Foundation of China, grant number 61703297, and the Shanxi Provincial Basic Research Program, grant number 20220302121153.

Institutional Review Board Statement: Not applicable.

Informed Consent Statement: Not applicable.

Data Availability Statement: The public supplementary package provides Data S1–S10 together with the original Python reproduction script (reproduce_submission_results.py), README, requirements, method note, reproduction summary and file manifest for the deterministic Noble–Abel analyses. The independent EOS addendum provides Data S11–S14B, software metadata and explanatory documentation for the stored model-derived fixed-state comparisons, pressure-boundary mappings, numerical checks, state classifications and SRH_{60} results. The EOS addendum does not include the original Stage 9.3 execution scripts and is not a portable, independently rerunnable EOS package. These materials are deterministic model outputs; the study provides no station field measurements or vehicle-side experimental measurements, and no new experimental data were collected.

Acknowledgments: During preparation and revision of this study, the authors used OpenAI ChatGPT primarily for research discussion, analysis, and suggestions, and also for research-workflow organization, manuscript and reviewer-response drafting and editing, and consistency checks. The authors made the final research-design decisions. During the revision-stage audit, OpenAI Codex was used to inspect archived code and data, reproduce documented deterministic calculations, compare numerical outputs, and prepare audit reports and logs. The available records do not establish a complete step-by-step attribution of every original regression and scheduling design, coding, execution, and interpretation task to a particular author or AI tool. The authors checked the equations, key numerical results, data, and model assumptions and retain responsibility for the scientific content, interpretations, and conclusions. The original MATLAB computational implementation used MATLAB R2024b (version 24.2.0.2712019). The original Python runtime version used for the Data S1–S10 package was not retained in the contemporaneous records; the accompanying scripts specify Python 3.10 or later. The separate EOS supplementary addendum was executed using Python 3.13.9 and CoolProp 8.0.0. The specific ChatGPT model identifier and OpenAI Codex software version used during the relevant preparation and revision period were not retained in the contemporaneous records.

Conflicts of Interest: The authors declare no conflicts of interest.

References

1. Xu, J.; Xie, H.; Huang, L.; Li, A.; Zhao, K.; Wang, Y. Event-triggered model predictive control for the cascade filling process of a hydrogen fuelling station. *Eng. Optim.* **2024**, *56*, 940–962. https://doi.org/10.1080/0305215x.2023.2212243.
2. Yu, Y.; Lu, C.; Ye, S.; Hua, Z.; Gu, C. Optimization on volume ratio of three-stage cascade storage system in hydrogen refueling stations. *Int. J. Hydrogen Energy* **2022**, *47*, 13430–13441. https://doi.org/10.1016/j.ijhydene.2022.02.086.

3. Luo, H.; Xiao, J.; Bénard, P.; Chahine, R.; Yang, T. Multi-objective optimization of cascade storage system in hydrogen refuelling station for minimum cooling energy and maximum state of charge. *Int. J. Hydrogen Energy* **2022**, *47*, 10963–10975. https://doi.org/10.1016/j.ijhydene.2022.01.059.
4. Xiao, L.; Chen, J.; Wu, Y.; Zhang, W.; Ye, J.; Shao, S.; Xie, J. Effects of pressure levels in three-cascade storage system on the overall energy consumption in the hydrogen refueling station. *Int. J. Hydrogen Energy* **2021**, *46*, 31334–31345. https://doi.org/10.1016/j.ijhydene.2021.07.007.
5. Reddi, K.; Elgowainy, A.; Sutherland, E. Hydrogen refueling station compression and storage optimization with tube-trailer deliveries. *Int. J. Hydrogen Energy* **2014**, *39*, 19169–19181. https://doi.org/10.1016/j.ijhydene.2014.09.099.
6. Genovese, M.; Fragiacomo, P. Hydrogen refueling station: Overview of the technological status and research enhancement. *J. Energy Storage* **2023**, *61*, 106758. https://doi.org/10.1016/j.est.2023.106758.
7. Chen, G.; Su, S.; Xu, Q.; Lv, H.; Zhao, Y.; Xia, L.; Zhang, G.; Hu, K. Optimization of hydrogen refueling strategy: Based on energy consumption and refueling demand. *Int. J. Hydrogen Energy* **2024**, *71*, 625–636. https://doi.org/10.1016/j.ijhydene.2024.05.167.
8. Hu, H.; Di, J.; Lang, Z.; Meng, Z.; Shi, X.; Du, *D.*; He, Q. Thermodynamic modeling and analysis of hydrogen storage systems in hydrogen refueling stations. *Int. J. Hydrogen Energy* **2024**, *57*, 1101–1110. https://doi.org/10.1016/j.ijhydene.2024.01.099.
9. Bai, Y.; Zhang, C.; Duan, H.; Jiang, S.; Zhou, Z.; Grouset, *D.*; Zhang, M.; Ye, X. Modeling and optimal control of fast filling process of hydrogen to fuel cell vehicle. *J. Energy Storage* **2021**, *35*, 102306. https://doi.org/10.1016/j.est.2021.102306.
10. Sadi, M.; Deymi-Dashtebayaz, M. Hydrogen refueling process from the buffer and the cascade storage banks to HV cylinder. *Int. J. Hydrogen Energy* **2019**, *44*, 18496–18504. https://doi.org/10.1016/j.ijhydene.2019.05.023.
11. Fragiacomo, P.; Martorelli, M.; Genovese, M.; Piraino, F.; Corigliano, O. Thermodynamic modelling, testing and sensitive analysis of a directly pressurized hydrogen refuelling process with a compressor. *Renew. Energy* **2024**, *226*, 120410. https://doi.org/10.1016/j.renene.2024.120410.
12. Yang, X.; Wang, W.; Wang, Z.; Ma, F. Simulation of pre-cooling in a high pressure hydrogen refueling station for operation optimization. *Int. J. Hydrogen Energy* **2024**, *86*, 434–444. https://doi.org/10.1016/j.ijhydene.2024.04.064.
13. Frolova, E.A.; Zhdaneev, O.V. Safety as a Driver of Technological Development in Hydrogen Refueling Stations Infrastructure. *Int. J. Hydrogen Energy* **2026**, *276*, 157508. https://doi.org/10.1016/j.ijhydene.2026.157508.
14. Oueslati, F. Optimizing Autonomous Hydrogen Refueling Stations in Tunisia: A Comparative Analysis of a Novel RFR-LSTM-ANN-HPC Framework versus HOMER Modeling. *Next Res.* **2026**, *10*, 101914. https://doi.org/10.1016/j.nexres.2026.101914.
15. Cardona, P.; Valiño, L.; Ocampo-Martínez, C.; Serra, M. Mixed logical dynamical modelling of renewable hydrogen refuelling stations for the design of optimization-based operational schemes. *Appl. Energy* **2025**, *393*, 126037. https://doi.org/10.1016/j.apenergy.2025.126037.
16. Liu, X.; Zu, L.; Wei, Z.; Wang, Y.; Pan, Z.; Xiao, G.; Jenkins, N. Two-layer optimal scheduling of integrated electric-hydrogen energy system with seasonal energy storage. *Int. J. Hydrogen Energy* **2024**, *82*, 1131–1145. https://doi.org/10.1016/j.ijhydene.2024.07.415.
17. Li, Z.; Xia, Y.; Bo, Y.; Wei, W. Optimal planning for electricity-hydrogen integrated energy system considering multiple timescale operations and representative time-period selection. *Appl. Energy* **2024**, *362*, 122965. https://doi.org/10.1016/j.apenergy.2024.122965.
18. Wei, P.; Cai, *D.*; Ukwuoma, C.C.; Li, L.; Bamisile, O.; Huang, Q. Optimal scheduling of an integrated electric-hydrogen-thermal energy system considering carbon trading and wind farm aggregation. *Int. J. Hydrogen Energy* **2025**, *97*, 1275–1286. https://doi.org/10.1016/j.ijhydene.2024.11.289.
19. Wang, Z.; Du, B.; Li, Y.; Xie, C.; Wang, H.; Huang, Y.; Meng, P. Multi-time scale scheduling optimization of integrated energy systems considering seasonal hydrogen utilization and multiple demand responses. *Int. J. Hydrogen Energy* **2024**, *67*, 728–749. https://doi.org/10.1016/j.ijhydene.2024.04.125.
20. Najafi, A.; Homaee, O.; Jasiński, M.; Tsaousoglou, G.; Leonowicz, Z. Integrating hydrogen technology into active distribution networks: The case of private hydrogen refueling stations. *Energy* **2023**, *278*, 127939. https://doi.org/10.1016/j.energy.2023.127939.
21. Pang, Y.; Pan, L.; Zhang, J.; Chen, J.; Dong, Y.; Sun, H. Integrated sizing and scheduling of an off-grid integrated energy system for an isolated renewable energy hydrogen refueling station. *Appl. Energy* **2022**, *323*, 119573. https://doi.org/10.1016/j.apenergy.2022.119573.
22. Shi, M.; Huang, Y. Dynamic planning and energy management strategy of integrated charging and hydrogen refueling at highway energy supply stations considering on-site green hydrogen production. *Int. J. Hydrogen Energy* **2023**, *48*, 29835–29851. https://doi.org/10.1016/j.ijhydene.2023.04.201.
23. Tang, Y.; Xun, Q.; Liserre, M.; Yang, H. Energy management of electric-hydrogen hybrid energy storage systems in photovoltaic microgrids. *Int. J. Hydrogen Energy* **2024**, *80*, 1–10. https://doi.org/10.1016/j.ijhydene.2024.07.017.

24. Nguyen, V.H.; Jeanmougin, A.; Lecointe, V.; Hammer, B. Hybrid edge–cloud energy management system for an industrial-scale green hydrogen refilling station: Lessons learned and findings. *Int. J. Hydrogen Energy* **2024**, *85*, 360–373. https://doi.org/10.1016/j.ijhydene.2024.08.151.
25. Huy, T.H.B.; Duy, N.T.M.; Van Phu, P.; Le, T.-*D*.; Park, S.; Kim, *D*. Robust real-time energy management for a hydrogen refueling station using generative adversarial imitation learning. *Appl. Energy* **2024**, *373*, 123847. https://doi.org/10.1016/j.apenergy.2024.123847.
26. Zhou, L.; Wei, X.; Suvorov, A.; Safaraliev, M. Operation of coupled power-gas networks with hydrogen refueling stations, responsive demands and storage systems: A novel stochastic framework. *Energy* **2024**, *309*, 133071. https://doi.org/10.1016/j.energy.2024.133071.
27. Yan, N.; Zhao, Z.; Li, X.; Yang, J. Multi-time scales low-carbon economic dispatch of integrated energy system considering hydrogen and electricity complementary energy storage. *J. Energy Storage* **2024**, *104*, 114514. https://doi.org/10.1016/j.est.2024.114514.
28. Wang, C.; Chen, S.; Zhao, J.; Zhou, Y.; Wei, Z.; Zheng, S. Coordinated scheduling of integrated electricity, heat, and hydrogen systems considering energy storage in heat and hydrogen pipelines. *J. Energy Storage* **2024**, *85*, 111034. https://doi.org/10.1016/j.est.2024.111034.
29. Zheng, J.; Li, L.; Chen, R.; Xu, P.; Kai, F. High Pressure Steel Storage Vessels Used in Hydrogen Refueling Station. *J. Press. Vessel Technol.* **2008**, *130*, 014503. https://doi.org/10.1115/1.2826453.
30. Leachman, J.W.; Jacobsen, R.T.; Penoncello, S.G.; Lemmon, E.W. Fundamental Equations of State for Parahydrogen, Normal Hydrogen, and Orthohydrogen. *J. Phys. Chem. Ref. Data* **2009**, *38*, 721–748. https://doi.org/10.1063/1.3160306.
31. Groth, K.; Hecht, E.; Reynolds, J. *Methodology for Assessing the Safety of Hydrogen Systems: HyRAM 1.0 Technical Reference Manual*; Sandia National Laboratories: Albuquerque, NM, USA, 2015; p. SAND2015-10216. https://doi.org/10.2172/1814840.
32. Bell, I.H.; Wronski, J.; Quoilin, S.; Lemort, V. Pure and Pseudo-pure Fluid Thermophysical Property Evaluation and the Open-Source Thermophysical Property Library CoolProp. *Ind. Eng. Chem. Res.* **2014**, *53*, 2498–2508. https://doi.org/10.1021/ie4033999.

Disclaimer/Publisher's Note: The statements, opinions and data contained in all publications are solely those of the individual author(s) and contributor(s) and not of MDPI and/or the editor(s). MDPI and/or the editor(s) disclaim responsibility for any injury to people or property resulting from any ideas, methods, instructions or products referred to in the content.